Energy & Environmental Science

High-performance magnesium metal battery via switching passivation film into solid electrolyte interphase

Journal:	*Energy & Environmental Science*
Manuscript ID	EE-COM-02-2021-000614.R3
Article Type:	Communication
Date Submitted by the Author:	10-Jun-2021
Complete List of Authors:	Bae, Jiwoong; The University of Texas at Austin, Mechanical Engineering Park, Hyoju; The University of Texas at Austin Guo, Xuelin; The University of Texas at Austin, Materials Science and Engineering Zhang, Xiao; University of Texas at Austin Warner, Jamie; The University of Texas at Austin Yu, Guihua; The University of Texas at Austin, Materials Science and Engineering

COMMUNICATION

High-performance magnesium metal battery via switching passivation film into solid electrolyte interphase

Received 00th January 20xx,
Accepted 00th January 20xx

DOI: 10.1039/x0xx00000x

Jiwoong Bae,‡ Hyoju Park,‡ Xuelin Guo, Xiao Zhang, Jamie H. Warner, and Guihua Yu *

Magnesium-ion battery has been regarded as a promising alternative to the lithium-ion battery due to its high theoretical capacity, relatively high potential, and magnesium abundance. However, the contradiction between the plating/stripping of Mg^{2+} and the electrolytes' oxidative stability has hampered the Mg-ion battery's development for energy storage applications. Here, we designed an amorphous MgO-wrapped Zn-skeleton as a unique current collector for an anode-free Mg battery to allow reversible Mg^{2+} plating/stripping in oxidatively stable electrolytes. The significant lattice mismatch between hexagonal Zn and MgO induces dislocations, leading to a highly defective interphase. Such layer behaves as a mixed ionic-electronic conductor, rendering Mg nanoparticles upon electroplating. Combined with a large surface area, the proposed current collector considerably improved charge transfer kinetics and lowered the cell impedance for Mg^{2+} plating/stripping by 1/20 of the typical Mg metal. Moreover, Mg^{2+} interphase conduction was facilitated by two orders of magnitude higher (~10^{-11} S cm^{-1}) than the widely known passivating layer (< 10^{-13} S cm^{-1}). This special design enables Mg-Li hybrid batteries with non-corrosive electrolytes to exhibit a high-operating-voltage of 2.82 V vs. Mg/Mg^{2+} and an energy density of 412.5 Wh kg^{-1}.

Broader context

Next-generation batteries have been explored for their unique merits including safe operation, non-toxicity, environmental-friendly materials, and earth-abundance. Solid-state electrolyte, Li-metal anode, conversion-based electrodes, and multivalent-ion batteries are the promising next-generation batteries. Among them, multivalent-ions, such as Al^{3+}, Zn^{2+}, Ca^{2+} and Mg^{2+}, are one of the widely studied chemistry as an alternative to Li-ion chemistry. However, the different valence state and ionic radius have caused unexpected problems such as slow diffusion in solid-state electrode or high desolvation energy in electrolyte. In addition, the different standard reduction potential of those multivalent-ions often limit the cell operating voltage, and thus lowering energy/power density of batteries. In this study, Mg-ion batteries have been investigated, particularly to solve the dilemma of electrolytes (i.e., difficulty to satisfy electrochemical compatibilities at both anode and cathode). We have employed interfacial chemistry and engineering at the anode current collector that enables high-voltage operation of Mg-ion batteries.

'Beyond lithium (Li)-ion batteries' has been a major research direction in recent years due to the physicochemical limit of Li-ion chemistry[1, 2] and the various issues such as safety problem, high-cost and scarcity of the core elements.[3] These limitations of Li-ion batteries have required the battery society to explore alternative materials and chemistry, including solid-state electrolytes,[4] Li-metal batteries,[5] liquid-metal batteries,[6] conversion-based electrodes[7], and multivalent-ion batteries.[8-11]

Among many candidates, magnesium (Mg) metal has attracted great attention due to the high theoretical capacity (3,833 mAh cm^{-3} and 2,205 mAh g^{-1}) and the low standard reduction potential (Mg/Mg^{2+} = -2.37 V vs. the standard hydrogen electrode (SHE)).[8] Mg is the 7th most abundant element in the earth's crust, which contains about 1,000 times more Mg (23,300 ppm) than Li (20 ppm) and is the 3rd most-used metal in the industry, which makes Mg a practically affordable element. Mg-metal is thermally stable (e.g., auto-ignition temperature is 473 °C for bulk Mg and 179 °C for Li) and chemically reliable in the air and water as a consequence of the self-passivating behavior forming MgO, $Mg(OH)_2$ or $Mg(OH)_2CO_3$ films.[12]

Nevertheless, the electrolyte dilemma between reversible Mg^{2+} plating/stripping and a high-voltage operation has been a major concern for Mg-ion batteries.[13] The ethereal organometallic Mg-ion electrolytes demonstrate a strong capability for the reversible Mg^{2+} plating/stripping (i.e., coulombic efficiency ~100%) owing to the absence of the

Materials Science and Engineering Program, Texas Materials Institute, The University of Texas at Austin, Austin, TX 78712, USA.
Email: ghyu@austin.utexas.edu (G.Y.)

†Electronic Supplementary Information (ESI) available. See DOI: 10.1039/x0xx00000x

‡These authors contributed equally to this work

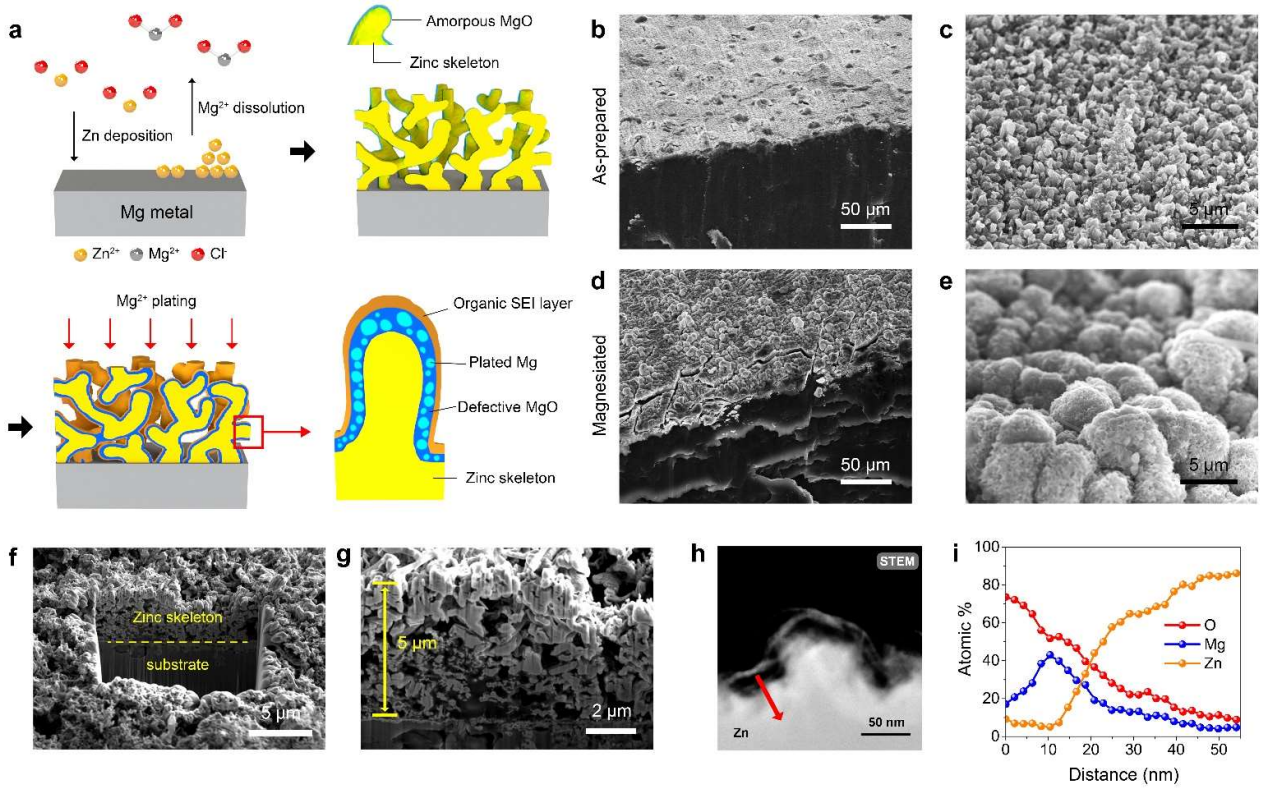

Fig. 1 (a) Schematic illustrations of Zn-skeleton preparation and following magnesiation. SEM images of (b) the cross-sectional and (c) the top surface of the as-prepared Zn-skeleton. SEM images of (d) the cross-sectional and (e) the top surface of the magnesiated Zn-skeleton. FIB-SEM images of (f) the beamed area and (g) the cross-sectional area of the Zn-skeleton after magnesiation. (h) STEM image and (i) EDX line profile of the cross-sectional magnesiated Zn-skeleton. The red arrow in (h) indicates the line scan area.

interphase between the electrode and the electrolyte.[14] However, these electrolytes are barely operable at a high-voltage (> 3 V vs. Mg/Mg^{2+}) originating from the oxidation vulnerability and the corrosive nature to the common cell components (e.g., layered oxides, stainless-steel or aluminum).[15] To address such an issue, various strategies have been developed. A recent study reported a method to resolve the passivating issue that an artificial protecting layer on Mg-metal may effectively enable Mg^{2+} plating/stripping in carbonate electrolytes.[16] A weakly coordinating electrolyte has also been developed in another work, which shows fast Mg^{2+} plating/stripping under a high current density.[17]

Despite all, non-corrosive conventional electrolytes have been considered the most attractive electrolyte due to the high oxidative stability and facile synthesis (a simple mixture of carbonate solvents (e.g., cyclic- or linear-carbonates) and common salts (e.g., $Mg(ClO_4)_2$ or $Mg(TFSI)_2$)), satisfy the requirements for the high-voltage cathode materials.[18] Unfortunately, the Mg-metal anode passivates itself in such electrolytes by forming a poorly conductive interphase and thus shutting down the electroplating. The ionic conductivity (e.g., ~10^{-15} S cm^{-1} for MgO) of such interphase is several orders lower than that of Li-ion battery (e.g., 10^{-7} ~ 10^{-10} S cm^{-1}), which drastically increases the cell impedance and hinders metal plating/stripping.[19, 20]

Besides, achieving high energy densities is still a challenging task for Mg-ion batteries as a consequence of the narrow cell voltages derived from the low redox potential of the Mg-based cathode[21, 22] and the intrinsically higher potential of the Mg-metal anode (Mg/Mg^{2+} is 0.67 V higher than Li/Li^{+}).[23] For instance, the operating voltage of Mg-metal | Mo_6S_8 is only 1.0 V, while that of Li-metal | Mo_6S_8 is as high as 2.1 V.[24, 25] Considering that the energy density (Wh kg^{-1}) is closely related to the capacity (Ah), the operating voltage (V) and the total weight of the battery (kg), developing a light-weight Mg-ion battery that stably operates at a high-voltage is important for practical applications.[26]

To overcome such limitations, we have designed an amorphous MgO wrapped Zn-skeleton as a unique current collector for an anode-free Mg-ion battery to enable Mg^{2+} plating/stripping in conventional electrolytes. The key approach of this study originates from a highly defective MgO layer on the Zn-skeleton. First, the Zn-skeleton exhibits a large surface area, offering abundant reaction sites for Mg^{2+} to deposit. Second, the significant lattice mismatch between hexagonal Zn and Mg/MgO induces a highly defective interphase with relatively faster charge transport. The spectroscopic studies confirmed abundant defects in the interphase, which showed a high conductivity and a low overpotential during the cycling process. Lastly, the Mg^{2+} ions are plated in the defective MgO interphase

due to the mixed ionic electronic conduction, rendering particle-like Mg morphology. Therefore, we could switch the widely known 'passivation film' into a 'solid electrolyte interphase (SEI) layer' in non-corrosive carbonate electrolytes by a facile control of the interfacial chemistry. Besides, the anode-free structure with a high-voltage operation can be a potential strategy to improve the energy density of Mg-ion batteries significantly. As a proof of concept, we have successfully demonstrated Mg-Li hybrid batteries with oxidatively-stable carbonate electrolytes, demonstrating a record high operating voltage 2.82 V vs. Mg/Mg^{2+} and an energy density of 412.5 Wh kg^{-1} based on the cathode weight. We believe that a high operating voltage with an anode-free interface may open the future direction of next-generation rechargeable Mg-ion batteries.

Magnesium plating on Zn-skeleton

An amorphous MgO wrapped Zn-skeleton was prepared on the Mg current collector to enable Mg^{2+} plating/stripping in non-corrosive carbonate electrolytes (Fig. 1a). To be specific, a surface-scratched Mg current collector was immersed in 1 M $ZnCl_2$ in tetrahydrofuran (THF) solution to coat a Zn-skeleton layer via a chemical conversion reaction that deposits Zn while dissolves Mg^{2+} into the solution.[27] It is believed that a significant amount of dissolved Mg^{2+} ions are precipitated to $MgCl_2$ due to the limited solubility of $MgCl_2$ in THF. During the reaction, an ultra-thin layer of amorphous MgO covers the Zn-skeleton. In the wake of the Mg^{2+} plating, the partial decomposition of electrolytes will lead to an organic SEI layer. Importantly, the amorphous and defective MgO layer will be placed between the organic SEI layer and Zn-skeleton. This defective MgO allows Mg^{2+} ions and electrons to conduct, and thus Mg may be deposited in this interphase.

The evolution of morphology during the magnesiation was investigated by scanning electron microscopy (SEM) (Fig. 1b-e). The as-prepared Zn-skeleton shows a thin and homogeneous porous Zn coated on the Mg current collector (Fig. 1b). It is also observed that the Zn-skeleton reveals a high-surface-area (Fig. 1c). The cross-sectional image confirms that the thickness is around 5 μm (Fig. S1, ESI†), and a well-attached Zn-skeleton on the Mg current collector was observed (Fig. S2, ESI†). The Zn-skeleton was magnesiated in 0.5 M magnesium perchlorate ($Mg(ClO_4)_2$) in propylene carbonate (PC) under 0.01 mA cm^{-2} for 35.6 hrs (0.356 mAh cm^{-2}). The magnesiated Zn-skeleton surface became corrugated as a consequence of the Mg electroplating (Fig. 1d). The deposited Mg on Zn-skeleton also renders dendrite-free morphology but smooth chunks with a size of 3 ~ 6 μm (Fig. 1e). The morphology and elemental distribution during the magnesiation can also be found from SEM images along with energy-dispersive X-ray spectroscopy (EDX) (Fig. S3, ESI†). The inner morphology was further investigated by a cross-sectional cutting with a focused ion beam (FIB) and SEM. In Fig. 1f, the beamed area displays the boundary between the Zn-skeleton and the Mg current collector. The enlarged cross-sectional view in Fig. 1g demonstrates that Zn-skeleton is highly porous but partially filled with plated Mg.

The compositional distribution has been analyzed by scanning transmission electron microscopy (STEM) with EDX. Fig. 1h demonstrates a cross-sectional STEM image of Zn-skeleton with plated Mg. The atomic percentages (atomic %) of O, Mg, and Zn were plotted from the outer surface to the inner side in Fig. 1i. Importantly, a high O atomic % was observed at the outer surface, which may indicate the organic SEI and MgO layer. As the scan comes into the inner side, the Mg content has been increased, followed by increasing Zn, implying that Mg has been successfully plated on the Zn-skeleton (The STEM-EDX elemental mapping can be found in Fig. S4, ESI†).

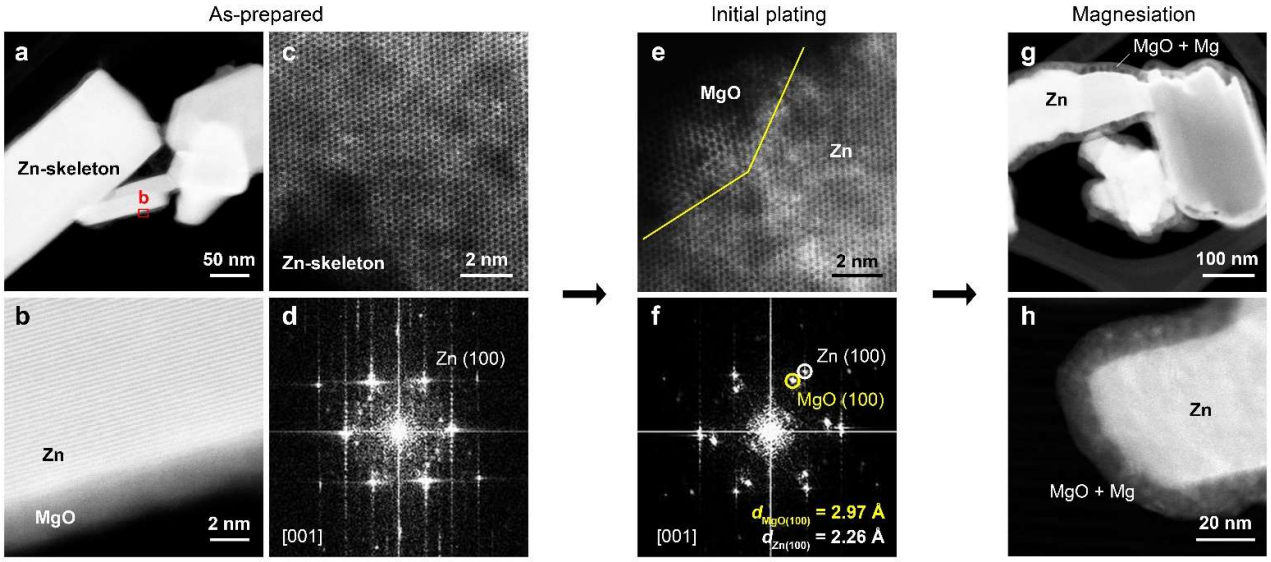

Fig. 2 (a,b) STEM and (c) HR-STEM images and (d) corresponding FFT pattern of the as-prepared Zn-skeleton. (e) HR-STEM image and (f) corresponding FFT pattern of the Zn-skeleton after initial plating. (g,h) TEM images of the magnesiated Zn-skeleton.

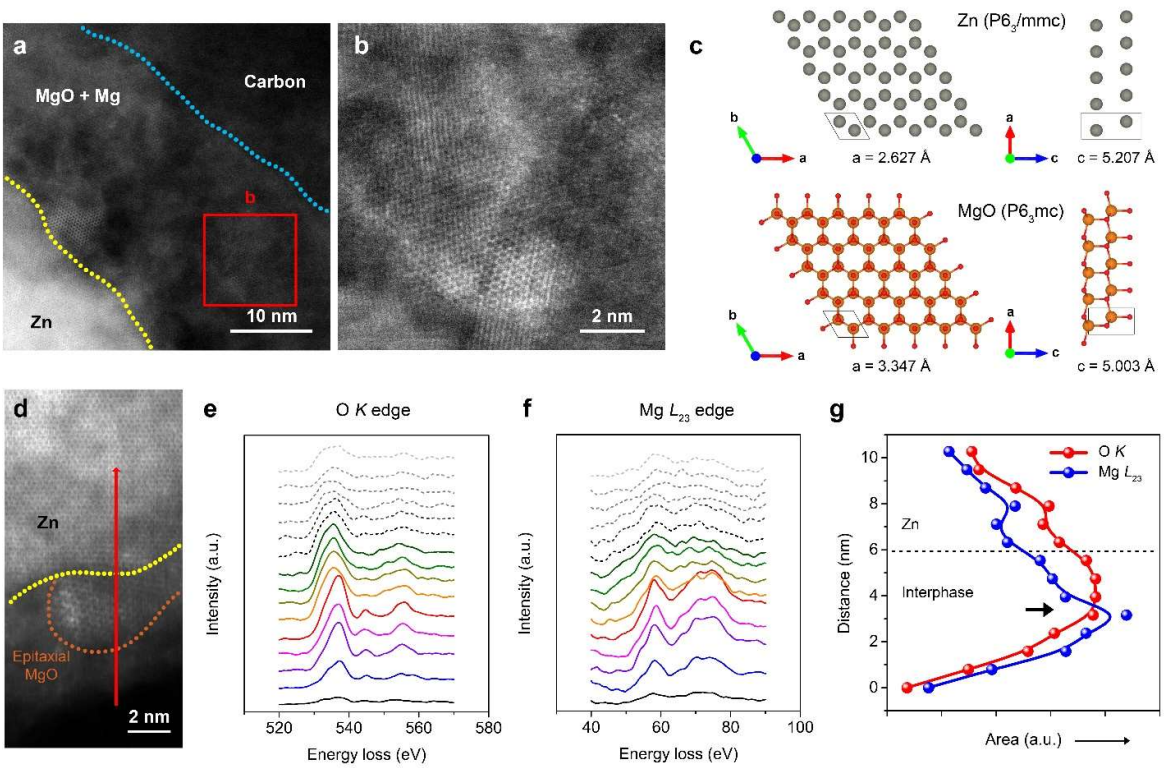

Fig. 3 (a) HR-STEM images of the interphase on the Zn-skeleton and (b) enlarged image. (c) The crystal structure of hexagonal Zn (P63/mmc) and MgO (P63mc). (d) STEM image and EELS spectra for (e) O K edge and (f) Mg L23 edge. (g) The area fitting of O K and Mg L23 edges with the distance.

Interphase on Zn- skeleton

A detailed analysis has been carried out to investigate the interphase layer's chemistry and composition during the initial Mg^{2+} plating process. STEM has been conducted on the as-prepared Zn-skeleton, as shown in Fig. 2a-d. First of all, it was interesting to see that Zn-skeleton has been covered by an ultra-thin (~2 nm) layer of amorphous MgO (Fig. 2a and b). Such an MgO layer is uniform throughout the whole Zn-skeleton (Fig. S5, ESI†). It is speculated that the amorphous MgO has been formed during the chemical conversion reaction by replacing Zn^{2+} with Mg^{2+} in the surface ZnO, forming amorphous MgO (The HR-STEM image and corresponding spectroscopic evidence of Zn and MgO layer can be found in Fig. S6, ESI†). The Zn-skeleton is highly crystalline hexagonal Zn metal, confirmed by the clear crystal structure in high-resolution (HR) STEM (Fig. 2c) and its fast Fourier transform (FFT) (Fig. 2d).

During the magnesiation, epitaxial MgO may form on the Zn-skeleton surface (Fig. 2e). Both Zn metal and MgO have a hexagonal crystal structure with a little twist angle that demonstrates a clear epitaxy in the FFT pattern (Fig. 2f). Nevertheless, the size of this epitaxial growth of MgO is very limited, leading to defective nanocrystalline MgO layers. Further magnesiation clearly renders a mixture of deposited Mg and MgO on the Zn-skeleton with a uniform thickness (Fig. 2g). The enlarged STEM image in Fig. 2h depicts the contrast variation for a mixture of MgO + Mg with a thickness of approximately 15 nm. It should be noted that the sample was washed by ethanol prior to the STEM analysis to remove the organic component for a clear display of the MgO + Mg interphase.

HR-STEM on the interphase has been conducted to see the interphase composition, as shown in Fig. 3a. The interphase is mainly composed of small nanocrystalline and amorphous MgO + Mg_xO_y + Mg showing a defective structure (Fig. 3b). These different phases are mixed in the interphase, and therefore the boundaries among them are overlapped. It also is inferred from the crystal structure of MgO and Zn in Fig. 3c that the huge lattice mismatch (i.e., $|d_{MgO(010)} - d_{Zn(010)}|/ d_{Zn(010)}$ = 31.4 %) between MgO ($d_{MgO(010)}$ = 2.97 Å) and Zn ($d_{Zn(010)}$ = 2.26 Å) causes severe dislocations to accommodate the strain induced by the large mismatch, leading to a highly defective structure.

Fig. 3d exhibits a STEM image where the interphase covers the Zn-skeleton surface. Along with the red arrow in Fig. 3d, the electron energy loss spectroscopy (EELS) has been conducted to investigate the different phases in the interphase. It should be noted that the line scan passes through the defective interphase, including epitaxial area (orange dotted line) and amorphous area (below the epitaxial area), as well as the

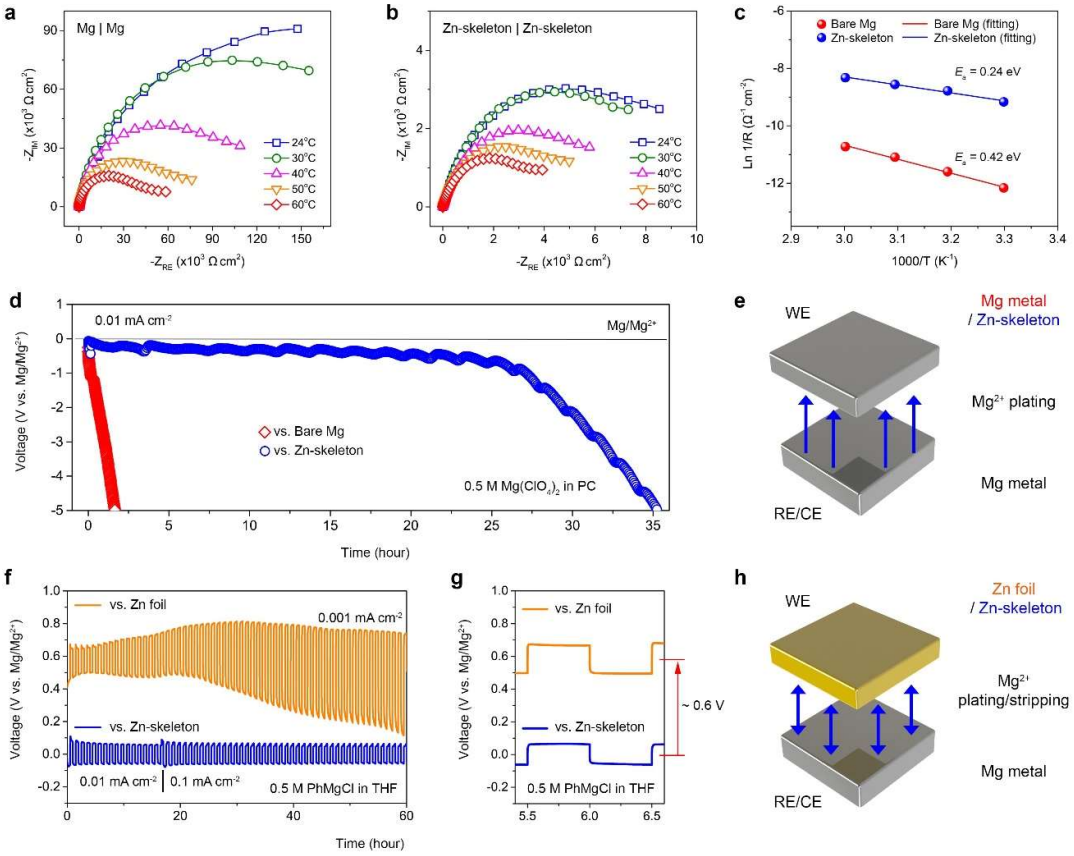

Fig. 4 EIS spectra of symmetric (a) bare Mg and (b) Zn-skeleton cells at different temperatures. (c) Arrhenius plot of 1/interfacial resistance (1/RInter) versus 1000/T. The inset values are the activation energies calculated from the Arrhenius relation. (d) The voltage profile and (e) schematic illustration of the Mg^{2+} plating on Mg metal or Zn-skeleton in 0.5 M $Mg(ClO_4)_2$ in PC electrolyte. (f) The cycling stability, (g) enlarged voltage profiles and h) schematic illustration of Mg^{2+} plating/stripping on Zn foil or Zn-skeleton in 0.5 M PhMgCl in THF electrolyte.

boundary between Zn and the interphase (yellow dotted line). It was shown in the O *K* edge (Fig. 3e) and Mg L_{23} edge (Fig. 3f) that the peaks are sharp on the epitaxial area while weak out of the crystal. The strong oxygen peaks indicate a crystalline structure without defects, while weaker peaks may imply the amorphous Mg or Mg_xO_y. To quantitatively compare, the O *K* edge and Mg L_{23} edge areas were measured and plotted in terms of the distance (Fig. 3g). The area ratios between the O *K* edge and Mg L_{23} edge are similar in the Zn area (< 6 nm), indicating there is not much difference in composition in the Zn area. However, in the interphase (0 ~ 6 nm), different compositions between O and Mg were observed. To be specific, the Mg L_{23} edge in epitaxial area (3 ~ 6 nm) exhibits a relatively smaller compared to that in the outer interphase (0 ~ 3 nm). Such a difference in terms of the area of EELS spectra may imply abundant defects (either Mg or O vacancy) in the interphase layer. It is believed that the defective and heterogeneous interphase generated during the initial magnesiation leads to the nanoparticle-like Mg morphology (Fig. S7, ESI†).

The chemical composition of the interphase was also investigated by X-ray photoelectron spectroscopy (XPS) after the symmetric cell cycling test in 0.5 M magnesium bis(trifluoromethanesulfonimide) ($MgTFSI_2$) in PC electrolyte for 10 cycles under 0.01 mA cm^{-2} for 30 min for each step (Fig. S8, ESI†). In the C1s spectrum of the bare Mg, typical organic or inorganic components were observed, such as CO_3 (291 eV), C=O (288 eV) and C-O (286.5 eV) (Fig. S8a, ESI†).[28, 29] A notable peak at 284 eV is C sp^2, mainly from the reduced organic species due to the electrolyte decomposition.[30, 31] A strong MgO peak (531 eV) from the O1s spectrum of bare Mg indicates the passivation layer's formation on the bare Mg (Fig. S8b, ESI†).[28, 29] In the case of C1s and O1s XPS spectra of Zn-skeleton, similar peaks were observed, but with significantly weaker C sp^2 peak (284 eV in Fig. S8c, ESI†) and MgO peak (531 eV in Fig. S8d, ESI†). Therefore, it can be inferred that Zn-skeleton effectively mitigated electrolyte decomposition and formed a compact interphase.

Electrochemical performance of symmetric Zn-skeleton cells

For the electrochemical cell test, an Mg powder electrode has been used. The morphology can be found in Fig. S9, ESI†. The symmetric cell impedances were investigated by

electrochemical impedance spectroscopy (EIS), as shown in **Fig. 4**a and b. Interestingly, the Zn-skeleton symmetric cell has much-reduced impedance compared to the Mg cell. Both bare Mg and the Zn-skeleton cells have comparable ohmic resistances (R_{Bulk} = 6.2 Ω cm^2 for bare Mg while 4.4 Ω cm^2 for Zn-skeleton at 24 ˚C), confirming that the notably reduced impedance of the Zn-skeleton cell is not from the conductivity difference of the electrolytes. On the contrary, the apparent difference was observed in the interfacial resistances where the bare Mg cell has an extremely large impedance of R_{Inter} = 167 kΩ cm^2 at 24 ˚C (Fig. 4a), whereas the Zn-skeleton cell shows R_{Inter} = 8 kΩ cm^2 at 24 ˚C (Fig. 4b), which is only ~1/20 of that of the bare Mg cell.

The reciprocal of interfacial resistance ($1/R_{Inter}$) was also investigated in the Arrhenius plot with increasing temperatures (Fig. 4c). It should be noted that the interfacial resistance (R_{Inter}) used in this study is attributed to both the charge carrier transport through the interphase (either passivation or SEI layer) and the charge transfer reaction. The Zn-skeleton demonstrated 3~4 orders higher $1/R_{Inter}$ value than bare Mg, confirming facile interfacial reactions. A notable difference was found not only from the magnitudes but also from the activation energies (E_a) of $1/R_{Inter}$ based on the Arrhenius relation, where a much lower value for Zn-skeleton (E_a = 0.24 eV) was observed compared to the bare Mg (E_a = 0.42 eV). The low activation energy implies the favorable ion transport and charge transfer of Mg^{2+} at the interphase. Based on the EIS fitting results, we have also estimated the interphase conductivities and thicknesses by the method using relaxation time associated with ion hopping (Fig. S10, ESI†). The details can be found in previous studies.[32, 33] The passivating interphase on bare Mg shows a very low conductivity of 2×10^{-13} S cm^{-1} with a thickness of 46 nm, which are expected due to the abundant passivating components on bare Mg, such as crystalline MgO[19]. By contrast, the Zn-skeleton cell demonstrates two orders of magnitude higher conductivity 2×10^{-11} S cm^{-1} and a very small thickness of 3.2 nm, implying the electrochemically favorable interphase. It is speculated that the abundant defects in the interphase of the Zn-skeleton may enhance the mixed ionic and electronic conductivity of MgO and thus facilitates charge carrier transport. A previous study showed an unexpectedly high electrical conductivity of MgO at room temperature due to "frozen-in" defects in oxides (i.e., non-equilibrium).[34]

The electrochemical behavior of Mg^{2+} plating/stripping has been investigated with symmetric Mg | Mg cells. The voltage profile was obtained from symmetric bare Mg and magnesiated Zn-skeleton cells with 0.5 M $Mg(ClO_4)_2$ in PC electrolytes (Fig. S11a, ESI†). As predicted, the bare Mg shows a rapidly increasing overpotential over 1 V due to the passivation layer's formation on the Mg-metal's bare surface. On the other hand, the symmetric Zn-skeleton cell demonstrates a very stable cycling performance with a much smaller overpotential (~30 mV). The overpotentials of the long-term cycling also confirm that the bare Mg cell is suffered from poor kinetics indicated by increasing overpotential over 4 V after 1000 hours of cycling (Fig. S11b, ESI†). On the contrary, the Zn-skeleton cell exhibits excellent long-term cycling stability with a considerably smaller overpotential (~70 mV after 1000 cycles). The Zn-skeleton cell can also be capable of Mg^{2+} plating/stripping at higher current densities up to 50 uA cm^{-2} for a longer plating time (Fig. S12, ESI†). The morphology change of the Zn-skeleton coated Mg powder electrode before/after magnesiation can be found in Fig. S13, ESI†.

To confirm the effectiveness of the facile Mg plating on the Zn-skeleton, we have also conducted a long-time magnesiation test (Fig. 4d). As shown in the schematic in Fig. 4e, Mg metal was used as reference/counter electrodes (RE/CE) while Mg-metal (red) or Zn-skeleton (blue) was used as a working electrode (WE). As expected, the bare Mg-metal shows a rapid increase in overpotential due to the passivation, which leads to 5 V in 3 hrs (vs. Bare Mg in Fig. 4d). Interestingly, the Zn-skeleton cell shows prolonged magnesiation over 35.6 hrs, proving the capability of a substantial amount of Mg^{2+} plating (vs. Zn-skeleton in Fig. 4d). The Zn-skeleton's wavy voltage profiles may stem from RE/CE (i.e., bare Mg metal), whose stripping process may cause unstable overpotentials in carbonate electrolytes.

In Fig. 4f-h, an additional experiment was also conducted in an asymmetric cell to see the role of amorphous MgO on Zn-skeleton, whose morphology was confirmed by STEM images (Fig. 2a and b). This time, Mg-metal foil was used as a RE/CE while a Zn foil or a Zn-skeleton as WE (Fig. 4h). 0.5 M phenyl magnesium chloride (PhMgCl) in THF was used as an electrolyte to enable Mg^{2+} plating/stripping at the RE/CE. First, it was noted that a long-term cycling test exhibited an increasing overpotential with the Mg | Zn cell even under a very low current density of 1 μA cm^{-2} (vs. Zn foil in Fig. 4f). Besides the large overpotential, a higher plating/stripping mid-voltage around 0.6 V vs. Mg/Mg^{2+} was observed, which is assumed to be an Mg-Zn alloying reaction (vs. Zn foil in Fig. 4g). In contrast, the Mg | Zn-skeleton cell shows a stable plating/stripping voltage profile under 10 μA cm^{-2} and 20 μA cm^{-2} for 70 hours (vs. Zn-skeleton in Fig. 4f). More importantly, the plating/stripping mid-voltage around 0 V vs. Mg/Mg^{2+} was observed, indicating that Mg^{2+} plating/stripping occurs on the Zn-skeleton surface instead of alloying reaction (vs. Zn-skeleton in Fig. 4g). The SEM image clearly shows the Mg deposition on top of the Zn-skeleton, where a distinct Mg layer was coated on the Zn-skeleton (Fig. S14, ESI†). Therefore, the Zn-skeleton on top of the Zn-skeleton may not work as a Zn^{2+} source nor Mg-Zn alloying host but only helps reversible Mg^{2+} plating/stripping. It is also important to mention that the pre-coated amorphous MgO on the Zn-skeleton plays a crucial role in the selective reaction of Mg-metal plating. The plating/stripping efficiency of Zn-skeleton in 0.5 M PhMgCl-THF electrolyte can be found in Fig. S15, ESI†.

A high-voltage magnesium-lithium hybrid battery

In order to verify the feasibility of our design, an Mg-Li hybrid battery has been investigated as a representative with 0.5 M $MgTFSI_2$ + 3 M lithium bis(trifluoromethanesulfonyl)imide (LiTFSI) in PC as an electrolyte. Due to the difficulty of finding a suitable high-voltage Mg cathode, $LiNi_{1/3}Co_{1/3}Mn_{1/3}O_2$ (NCM) was used as a cathode, which stably operates under a cut-off

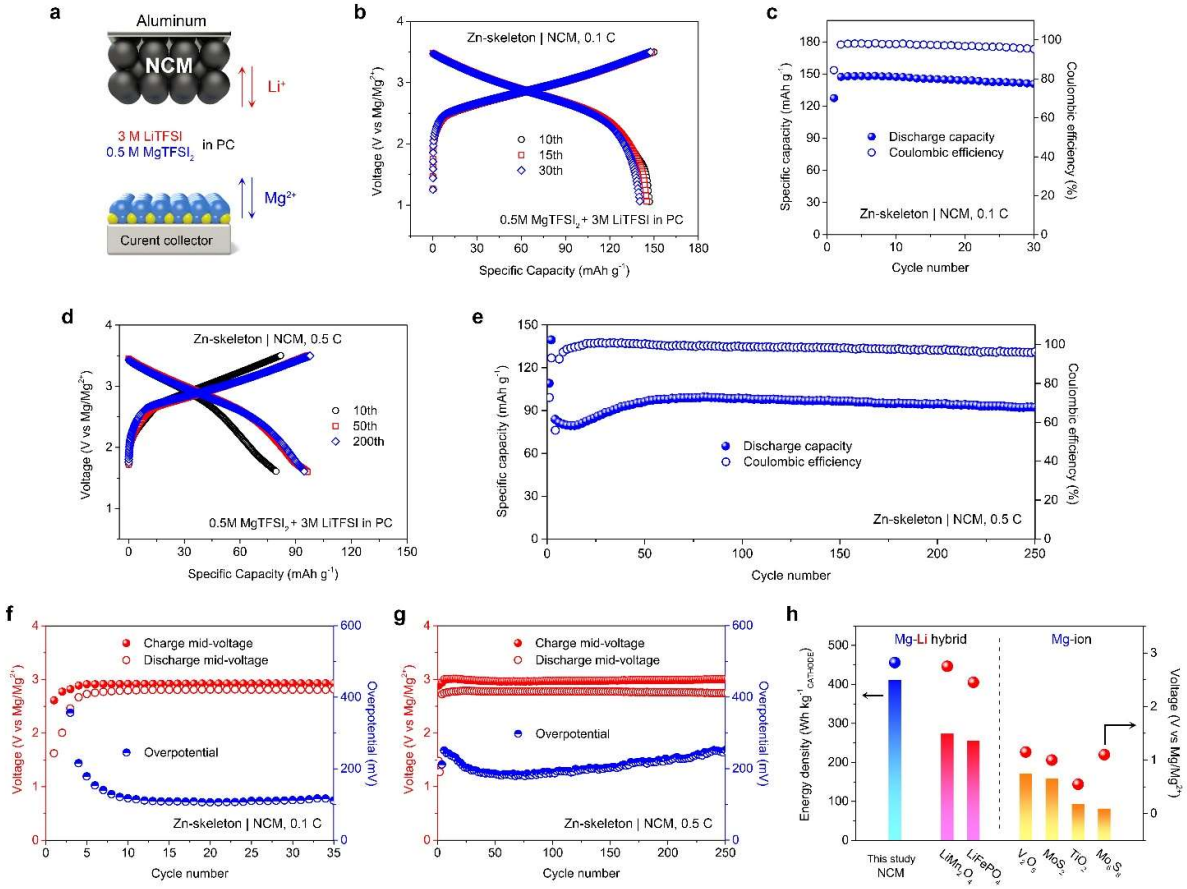

Fig. 5 (a) Schematic illustration of the Mg-Li hybrid battery. (b,d) Charge/discharge voltage profiles and (c,e) cycling performances of Mg-Li hybrid batteries with a Zn-skeleton anode and an NCM cathode at 0.1 C (b,c) and 0.5 C (d,e). Charge/discharge mid-voltage plot of Zn-skeleton | NCM batteries at (f) 0.1 C and (g) 0.5 C. (h) Energy densities calculated based on the weight of the cathode active materials.

voltage of 4.25 V vs. Li/Li$^+$. In this configuration, Mg^{2+} ions will be plated/stripped at the Zn-skeleton, while Li^+ ions will intercalate/deintercalate at the NCM cathode (Fig. 5a). Importantly, commercial aluminum (Al) foil was used as a current collector. It should be noted that Al could not be used in the conventional Mg electrolytes because of their corrosive nature (i.e., dissolution of Al^{3+} during the charging process)[15]. Fig. 5b shows charge-discharge voltage profiles of the Zn-skeleton | NCM battery with a cut-off voltage of 3.5 V vs. Mg/Mg^{2+} (4.17 V vs. Li/Li$^+$). A comparable specific capacity to Li-ion battery (Li | NCM ~150 mAh g^{-1}) was obtained with a stable cycling performance over 30 cycles at 0.1 C (Fig. 5c). The Zn-skeleton | NCM battery also showed the capability of a higher C-rate at 0.5 C (Fig. 5d) with excellent long-term cycling stability (Fig. 5e) over 250 cycles, implying the Zn-skeleton anode's reliability in practical applications. A high coulombic efficiency of 95 % was obtained for Zn-skeleton | NCM battery at the end of the cycling test. The carbonate electrolytes are more stable against oxidation, but still may cause corrosion at high voltage (> 3 V), lowering efficiency (Fig. S16, ESI†). In addition, It should be noted that our cell is an anode-free structure, where the efficiency is generally lower than a full cell. For instance, conventional Li-ion electrolyte shows lower than 90% Coulombic efficiency with an anode-free design.[35] After discharge (i.e., magnesiated cathode), the NCM cathode was investigated by SEM-EDX, which confirmed Li$^+$ intercalation at the cathode (Fig. S17, ESI†).

The charge-/discharge-mid voltages at 0.1 C were plotted in Fig. 5f, which shows stable values over 30 cycles with a low overpotential of ~100 mV. During the initial cycling, Mg^{2+} may prefer Mg-Zn alloying reaction to Mg-metal plating, which results in lower charge-/discharge-mid voltages (1st to 5th cycles). However, after the 5th cycle, the voltages increased to 2.82 V vs. Mg/Mg^{2+}, indicating a stable interphase layer formed, enabling reversible Mg^{2+} plating/stripping. The low redox potentials (< 0.4 V vs. Li/Li$^+$) of different alloying reactions also prove Mg/Mg^{2+} chemistry at the anode (Fig. S18, ESI†). To the best of our knowledge, this is the highest discharge-mid-voltage among the previously reported Mg-ion batteries. The charge-/discharge-mid-voltage of 0.5 C was plotted in Fig. 5g, demonstrating a stable and high discharge-mid voltage close to 2.8 V vs. Mg/Mg^{2+} with an overpotential of 200 mV. A control cell with Li-metal as anode and NCM cathode (Li | NCM battery) was also tested in the hybrid electrolyte. The Li | NCM battery

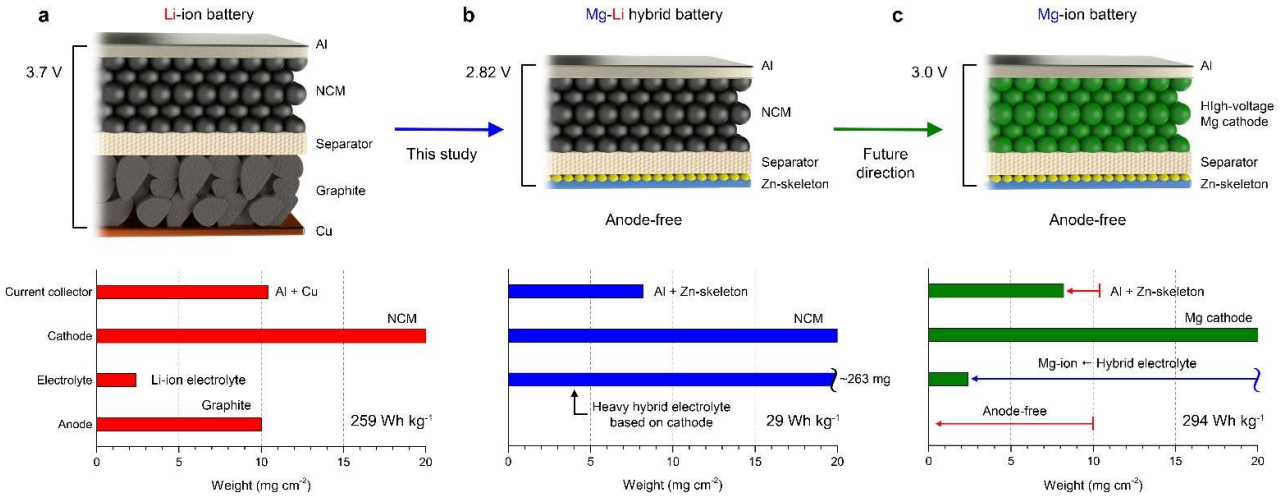

Fig. 6 Theoretical energy densities of (a) a conventional graphite | NCM battery, (b) a Zn-skeleton | NCM hybrid battery and (c) a Zn-skeleton | Mg cathode battery. The energy densities were calculated based on the total weight of a battery, including current collector, active materials, and electrolyte with separator.

showed poor cycling stability (Fig. S19, ESI†) and increasing overpotentials over cycling (Fig. S20, ESI†), which emphasizes the superior role of Zn-skeleton in Mg-Li hybrid batteries.

Additinal investigation on the Zn-skeleton in different electrolytes (i.e., Mg-Li hybrid electrolyte or Li ion electrolyte) has been conducted (Fig. S21, ESI†). The interphase of Zn-skeleton in the hybrid electrolyte clearly showed carboneceous/organic outer layer, Mg/MgO layer and Zn-skeleton, which is well agreed with our expectation in Fig. 1a. We also confirmed Mg nanocrystals in the interphase, confirming the role of mixed ionic/electronic conductor of the amorphous/defective MgO layer (Fig. S22, ESI†).

Based on the discharge-mid-voltage and the cathode's active material, the energy densities were calculated and compared with various Mg-ion and Mg-Li hybrid batteries (Fig. 5h). Due to the higher potential of Mg/Mg^{2+} (0.67 V higher than that of Li/Li^{+}) and sluggish Mg^{2+} diffusion in cathodes, most of the Mg-ion cathodes operable in traditional ethereal Mg electrolytes (oxidative stability < 3 V vs. Mg/Mg^{2+}) result in low energy densities: 172.5 Wh kg^{-1} (V_2O_5)[16], 160 Wh kg^{-1} (MoS_2),[36] 93.5 Wh kg^{-1} (TiO_2),[37] and 82.5 Wh kg^{-1} (Mo_6S_8).[38] In the previously reported Mg-Li hybrid battery studies, larger energy densities could be achieved due to the higher operating voltage of Li-ion cathodes: 275 Wh kg^{-1} ($LiMn_2O_4$)[39] and 257.3 Wh kg^{-1} ($LiFePO_4$).[40] Compared to the previous reports, our Zn-skeleton | NCM battery at 0.1 C demonstrated a remarkably higher energy density of 412.5 Wh kg^{-1}, which is more than doubled the energy density (< 172.5 Wh kg^{-1}) of the reported Mg batteries and even comparable to the energy density (~550 Wh kg^{-1}) of Li-ion battery (graphite | NCM).

The Mg-ion battery's lower operating voltage has been a major drawback to achieve a high energy density. Here, we propose a high-voltage Mg-ion battery with an anode-free design that can significantly increase the energy density. Unlike the Li-metal batteries, where severe electrolyte decomposition and dendritic/dead lithium growth at the anode lower the battery efficiency,[35] Mg-metal enables more stable and reversible metal plating/stripping owing to the low diffusion barrier of Mg^{2+} ions on the Mg-metal surface rendering dendrite-free morphology.[41]

The exemplary battery structure and their theoretical energy densities are demonstrated in Fig. 6a-c. Conventional Li-ion batteries with NCM cathode (e.g., 20 mg cm^{-2}) need to be inevitably combined with graphite anode (e.g., 1/2 weight of cathode), which yields the energy density of 259 Wh kg^{-1} (Fig. 6a). In the Zn-skeleton | NCM battery, the lower operating voltage (2.82 V) than the Li-ion battery (3.7 V) as well as the hybrid electrolyte results in a smaller energy density (Fig. 6b). It should be noted that the Zn-skeleton | NCM battery requires an Mg-Li hybrid electrolyte, which is proportional to the weight of the cathode. Therefore, if a high-voltage Mg-based cathode is assumed, the energy density could be boosted to 294 Wh kg^{-1}, beyond Li-ion batteries (Fig. 6c). We believe that pursuing the light-weight (e.g., anode-free) and the high-voltage and -capacity cathodes could be a promising direction for future research of Mg-ion batteries.[42]

Conclusions

A dilemma between Mg^{2+} plating/stripping at the anode and oxidative stability at the cathode has hampered Mg-ion batteries in achieving high energy density for practical applications. This study has shown an amorphous MgO-wrapped Zn-skeleton as a unique current collector for anode-free Mg battery to allow reversible Mg^{2+} plating/stripping. The lattice mismatch between Zn-skeleton and MgO induces a

highly defective MgO layer. Such a layer exhibits a fast charge carrier transport and facilitates Mg^{2+} ion plating due to the interphase layer's abundant defects. Owing to the anode interphase's fast kinetics and superior stability, we could construct Mg-Li hybrid batteries with oxidation-resistant electrolytes, enabling a high-voltage operation. The Mg-Li hybrid battery demonstrated excellent electrochemical performance with a record-high operating voltage of 2.82 V vs. Mg/Mg^{2+} and an energy density of 412.5 Wh kg^{-1} by the cathode. It is believed that this strategy can be generalized to broader applications, including metal-based batteries, by manipulating the interfacial chemistry between the host materials and the electroplating of metal ions.

Author contributions

G.Y. conceived and supervised the project. J.B. and H.P. designed experiments and co-wrote the manuscript. J.B., X.G. and X.Z. performed materials fabrication and characterization. H.P. and J.H.W. carried out electron microscopy and analysis. All the authors discussed the results and commented on the manuscript.

Conflicts of interest

The authors declare no competing financial interests.

Acknowledgements

G.Y. acknowledges the funding support from US Department of Energy, Office of Science, Basic Energy Sciences, under Award DE-SC0019019, and Camille Dreyfus Teacher-Scholar Award.

Notes and references

1. J. Janek and W. G. Zeier, *Nat. Energy*, 2016, **1**, 16141.
2. J. B. Goodenough and K.-S. Park, *J. Am. Chem. Soc.*, 2013, **135**, 1167-1176.
3. R. Schmuch, R. Wagner, G. Hörpel, T. Placke and M. Winter, *Nat. Energy*, 2018, **3**, 267-278.
4. S. Xin, Y. You, S. Wang, H.-C. Gao, Y.-X. Yin and Y.-G. Guo, *ACS Energy Lett.*, 2017, **2**, 1385-1394.
5. D. Lin, Y. Liu and Y. Cui, *Nat. Nanotechnol.*, 2017, **12**, 194.
6. X. Guo, L. Zhang, Y. Ding, J. B. Goodenough and G. Yu, *Energy Environ. Sci.*, 2019, **12**, 2605-2619.
7. Q. Li, H. Li, Q. Xia, Z. Hu, Y. Zhu, S. Yan, C. Ge, Q. Zhang, X. Wang, X. Shang, S. Fan, L. Gu, G. Miao, G. Yu and J. Moodera, *Nat. Mater.*, 2021, **20**, 76-83.
8. J. Muldoon, C. B. Bucur and T. Gregory, *Chem. Rev.*, 2014, **114**, 11683-11720.
9. T. Lu, Z. Zhang, B. Chen, S. Dong, C. Wang, A. Du, L. Wang, J. Ma and G. Cui, *Mater. Today Energy*, 2020, **17**, 100450.
10. M. Asif, M. Rashad, Z. Ali, H. Qiu, W. Li, L. Pan and Y. Hou, *Mater. Today Energy*, 2018, **10**, 108-117.
11. X. Xu, D. Chao, B. Chen, P. Liang, H. Li, F. Xie, K. Davey and S.-Z. Qiao, *Angew. Chem. Int. Ed.*, 2020, **59**, 21728-21735.
12. R. Lindström, L.-G. Johansson, G. E. Thompson, P. Skeldon and J.-E. Svensson, *Corros. Sci.*, 2004, **46**, 1141-1158.
13. H. D. Yoo, I. Shterenberg, Y. Gofer, G. Gershinsky, N. Pour and D. Aurbach, *Energy Environ. Sci.*, 2013, **6**, 2265-2279.
14. D. Aurbach, G. S. Suresh, E. Levi, A. Mitelman, O. Mizrahi, O. Chusid and M. Brunelli, *Adv. Mater.*, 2007, **19**, 4260-4267.
15. Y.-S. Guo, F. Zhang, J. Yang, F.-F. Wang, Y. NuLi and S.-I. Hirano, *Energy Environ. Sci.*, 2012, **5**, 9100-9106.
16. S.-B. Son, T. Gao, S. P. Harvey, K. X. Steirer, A. Stokes, A. Norman, C. Wang, A. Cresce, K. Xu and C. Ban, *Nat. Chem.*, 2018, **10**, 532-539.
17. H. Dong, O. Tutusaus, Y. Liang, Y. Zhang, Z. Lebens-Higgins, W. Yang, R. Mohtadi and Y. Yao, *Nat. Energy*, 2020, **5**, 1043-1050.
18. K. Xu, *Chem. Rev.*, 2004, **104**, 4303-4418.
19. F. Freund, M. M. Freund and F. Batllo, *J. Geophys. Res. Solid Earth*, 1993, **98**, 22209-22229.
20. E. Peled, *J. Power Sources*, 1983, **9**, 253-266.
21. M. Mao, T. Gao, S. Hou and C. Wang, *Chem. Soc. Rev.*, 2018, **47**, 8804-8841.
22. Z. Zhang, S. Dong, Z. Cui, A. Du, G. Li and G. Cui, *Small Methods*, 2018, **2**, 1800020.
23. R. Attias, M. Salama, B. Hirsch, Y. Goffer and D. Aurbach, *Joule*, 2019, **3**, 27-52.
24. E. Lancry, E. Levi, Y. Gofer, M. Levi, G. Salitra and D. Aurbach, *Chem. Mater.*, 2004, **16**, 2832-2838.
25. P. J. Mulhern and R. R. Haering, *Can. J. Phys.*, 1984, **62**, 527-531.
26. J. Liu, Z. Bao, Y. Cui, E. J. Dufek, J. B. Goodenough, P. Khalifah, Q. Li, B. Y. Liaw, P. Liu, A. Manthiram, Y. S. Meng, V. R. Subramanian, M. F. Toney, V. V. Viswanathan, M. S. Whittingham, J. Xiao, W. Xu, J. Yang, X.-Q. Yang and J.-G. Zhang, *Nat. Energy*, 2019, **4**, 180-186.
27. Z. Tu, S. Choudhury, M. J. Zachman, S. Wei, K. Zhang, L. F. Kourkoutis and L. A. Archer, *Nat. Energy*, 2018, **3**, 310-316.
28. Y. Gofer, R. Turgeman, H. Cohen and D. Aurbach, *Langmuir*, 2003, **19**, 2344-2348.
29. H. Kuwata, M. Matsui and N. Imanishi, *J. Electrochem. Soc.*, 2017, **164**, A3229-A3236.
30. D. Bar-Tow, *J. Electrochem. Soc.*, 1999, **146**, 824.
31. J. M. Vollmer, L. A. Curtiss, D. R. Vissers and K. Amine, *J. Electrochem. Soc.*, 2004, **151**, A178.
32. I. M. Hodge, M. D. Ingram and A. R. West, *J. Electroanal. Chem.*, 1976, **74**, 125-143.
33. W. Liu, S. W. Lee, D. Lin, F. Shi, S. Wang, A. D. Sendek and Y. Cui, *Nat. Energy*, 2017, **2**, 17035.
34. J. G. Smith, J. Naruse, H. Hiramatsu and D. J. Siegel, *Chem. Mater.*, 2017, **29**, 3152-3163.
35. J. Qian, B. D. Adams, J. Zheng, W. Xu, W. A. Henderson, J. Wang, M. E. Bowden, S. Xu, J. Hu and J.-G. Zhang, *Adv. Funct. Mater.*, 2016, **26**, 7094-7102.
36. C.-J. Hsu, C.-Y. Chou, C.-H. Yang, T.-C. Lee and J.-K. Chang, *Chem. Commun.*, 2016, **52**, 1701-1704.
37. T. Koketsu, J. Ma, B. J. Morgan, M. Body, C. Legein, W. Dachraoui, M. Giannini, A. Demortière, M. Salanne, F. Dardoize, H. Groult, O. J. Borkiewicz, K. W. Chapman, P. Strasser and D. Dambournet, *Nat. Mater.*, 2017, **16**, 1142-1148.

38. D. Aurbach, Z. Lu, A. Schechter, Y. Gofer, H. Gizbar, R. Turgeman, Y. Cohen, M. Moshkovich and E. Levi, *Nature*, 2000, **407**, 724-727.
39. B. Pan, Z. Feng, N. Sa, S.-D. Han, Q. Ma, P. Fenter, J. T. Vaughey, Z. Zhang and C. Liao, *Chem. Commun.*, 2016, **52**, 9961-9964.
40. Z. Zhang, H. Xu, Z. Cui, P. Hu, J. Chai, H. Du, J. He, J. Zhang, X. Zhou, P. Han, G. Cui and L. Chen, *J. Mater. Chem. A*, 2016, **4**, 2277-2285.
41. M. Jäckle, K. Helmbrecht, M. Smits, D. Stottmeister and A. Groß, *Energy Environ. Sci.*, 2018, **11**, 3400-3407.
42. Y. Kuang, C. Chen, D. Kirsch and L. Hu, *Adv. Energy Mater.*, 2019, **9**, 1901457.